





Unique design approach to realize an O-band laser monolithically integrated on 300 mm Si substrate by nano-ridge engineering

DAVIDE COLUCCI,^{1,2,*}  MARINA BARYSHNIKOVA,² YUTING SHI,¹ YVES MOLS,² MUHAMMAD MUNEEB,¹ YANNICK DE KONINCK,² DIDIT YUDISTIRA,² MARIANNA PANTOUVAKI,² JORIS VAN CAMPENHOUT,² ROBERT LANGER,² DRIES VAN THOURHOUT,¹  AND BERNARDETTE KUNERT²

¹Photonics Research Group, Ghent University-imec, Technologiepark-Zwijnaarde 126, 9052 Gent, Belgium

²imec, Kapeldreef 75, 3001 Heverlee, Belgium

*Davide.Colucci@UGent.be

Abstract: We introduce a new design space for optimizing III-V devices monolithically grown on Silicon substrates by extending the concept of nano-ridge engineering from binary semiconductors such as GaAs, InAs and GaSb to the ternary alloy InGaAs. This allows controlling the fundamental lattice constant of the fully relaxed ternary nano-ridge which thereby serves as a tunable base for the integration of diverse device hetero-layers. To demonstrate the flexibility of this approach, we realized an O-band nano-ridge laser containing three In_{0.45}Ga_{0.55}As quantum wells, which are pseudomorphically strained to an In_{0.25}Ga_{0.75}As nano-ridge base. The demonstration of an optically pumped nano-ridge laser operating around 1300 nm underlines the potential of this cost-efficient and highly scalable integration approach for silicon photonics.

© 2022 Optica Publishing Group under the terms of the [Optica Open Access Publishing Agreement](#)

1. Introduction

The silicon photonics industry strongly grew over the last decades and is moving towards volume production due to the increasing demand for high-speed optical transceivers in data centers. The key advantage of silicon photonics is the possibility to integrate various optical devices on large-scale Si wafers with a high fabrication maturity based on the CMOS process technology. This leads to an improved yield, increased scalability, more complex functionalities, and/or reduced costs in comparison to conventional modular or InP-based photonic integrated circuits (PICs).

In addition to optical interconnects [1–3] silicon photonics is rapidly making inroads in a variety of sensing applications, such as light detection and ranging (LIDAR), biosensors, and spectrometers [4–8]. For these applications, a substantial cost is typically associated with the required short-wave infrared laser sources, often preventing the wide-spread adoption in cost-sensitive markets.

As such, the integration of III-V devices, such as lasers and amplifiers, plays an important role in designing future silicon photonics integrated circuits, meeting the high requirements regarding device density and production cost. Currently such III-V devices or active III-V layers are transferred via flip-chip technique or are bonded to the silicon photonic chip in a so-called hybrid or heterogenous integration approach, respectively [9–13]. The monolithic growth of III-V layers directly on Si substrates would provide a clear advantage concerning device scalability, integration density and cost but it suffers from misfit defect formation in the active III-V layers leading to fast device performance degradation and failure. This defect formation is caused by the lattice mismatch between Si and III-V compound materials and the difference in their thermal expansion coefficients. Over the last four decades various hetero-epitaxial approaches

to control and confine the defect formation when depositing III-V on Si have been investigated. A straightforward method is the growth of a strain relaxed buffer (SRB) on a blanket Si wafer including optimized buffer gradients, defect filter layers and/or thermal annealing treatments [14–19]. To date, it is still very challenging to achieve a low enough threading dislocation density in the active III-V layer for the integration of a reliable laser diode with an acceptable buffer thickness ($\ll 3 \mu\text{m}$). However, the interest in SRB growth has recently risen again by the demonstration of a III-V quantum dot (QD) laser with an impressive long extrapolated device lifetime [20,21] caused by the higher tolerance of QD lasers to the destructive impact of threading dislocations in comparison to multi-quantum well lasers [22–24].

Another hetero-epitaxial integration approach for III-V layers on Si, which has gained a lot of interest over the last years, is based on selective area growth (SAG) on patterned Si wafers [16,25–31]. Advantages are efficient aspect ratio trapping (ART) of misfit defects (MDs) due to the growth of the mismatched materials inside highly confined structures, less issues with wafer warping and crack formation due to the restricted III-V coverage of the Si surface and reduced precursor consumption as the III-V material is only deposited where it is needed on the wafer as predefined by the pattern layout. The main disadvantage is the limited III-V volume and surface area being available for device integration, which is intrinsically linked to SAG applying a highly confined pattern. Device architectures have to be adjusted to (sub-) micrometer scaled cross section, which brings both advantages and challenges in the design of efficient III-V silicon photonic components.

Nano-ridge engineering (NRE) is a novel integration approach introduced by imec [32–34]. It is based on SAG and ART inside narrow trenches but includes the continuous III-V growth out of the trench to engineer a larger nano-ridge (NR) for device integration. The main benefit of NRE is the possibility to significantly increase the NR volume and, simultaneously, to efficiently trap the defects inside narrow trenches. At the same time the active device region, as part of the NR, is clearly separated from the area of relaxation inside the trench pattern, which is important to reduce the detrimental effect of misfit defects on device performance and lifetime.

The first device demonstration based on NRE was an optically pumped distributed feedback (DFB) laser emitting at 1020 nm [35] whereby the NR, several hundred nanometers in cross-section dimension, functions as a waveguide. This demonstration inspired new integration concepts, e.g., evanescent light coupling from the NR laser to a common Si waveguide fabricated on a SOI (Si-On-Insulator) wafer [36]. Currently, different contact approaches are under investigation to extract or inject electron-hole pairs. This consideration has led to a new loss-coupled DFB laser concept using a metal grating instead of an etched grating [37]. Room temperature lasing was demonstrated with an even improved threshold pump intensity in comparison to the first etched DFB NR lasers, which indicates that this metal grating could be an interesting approach for current injection. A different approach based on a 300 mm wafer-scale device process was reported by Ozdemir et al. [38]. Isolated small metal plugs are fabricated on top of the NRs as a cathode and another set of larger contact plugs are integrated on the Si buffer as an anode. A clear diode behavior was observed with very low dark current and a high responsivity at 1020 nm ($2 \cdot 10^{-8} \text{ A/cm}^2$ and 0.65 A/W at 1 V), emphasizing the high III-V crystal quality.

NRE is not only limited to GaAs since it was previously reported for InAs and GaSb [34,39] but can also be applied to ternary alloys such as InGaAs [40]. This leads to an entirely new design space as the fundamental lattice constant of the device hetero-structure is no longer limited to that of binary III-V semiconductors but can be adjusted by the monolithic integration of a fully relaxed ternary NR with a variable composition. In this paper, we will present a very first example of this concept.

In our first NR laser demonstration emitting at 1020 nm, the active gain region consists of an InGaAs/GaAs multi-quantum-well (MQW) structure with about 20% In. To shift the emission wavelength into the O-band (1260-1360 nm), the In-content of the MQW structure must be

increased beyond 40%, but, due to the large lattice mismatch, the pseudomorphic growth of such an In-rich multi-layer stack on top of a fully relaxed GaAs NR base is no longer possible without any misfit defect formation.

In a completely new device concept, an InGaAs NR with an In-concentration of 20-35% was deposited on a trench-patterned Si substrate. As a result, the lattice constant of the original GaAs NR base was increased by the incorporation of In to reduce the lattice-mismatch towards InGaAs QWs with 40-50% In. This ternary NR base is fully relaxed and provides a free-standing lattice constant of the InGaAs NR alloy, which is now used as a misfit defect free base for the In-rich MQWs deposition. Comparable to our first laser generation based on GaAs NRs, the complete InGaAs NR multi-layer stack was surrounded with an InGaP cap where the In-content had to be increased to be lattice matched to the new InGaAs NR base.

In a first iteration we investigated two different hetero-structures designed to achieve an efficient photoluminescence (PL) peak in the O-band. Based on a detailed study of these first samples, an optimized third hetero-structure was used for processing a metal loss-coupled DFB NR laser. Optically pumped laser operation emitting around 1300 nm highlights the excellent III-V crystal quality of this novel laser concept for the monolithic integration with silicon photonics. This very first device demonstration based on a freely chosen base lattice constant is an important milestone towards new device architectures that are made possible by NRE.

2. Experimental section

All three NR samples discussed in this paper were grown by metal organic vapor phase epitaxy (MOVPE) on trench-patterned 300 mm exactly oriented (001) Si substrates applying common liquid metal-organic precursors. Every die on the Si wafer contains various trench arrays in [110] and [-110] directions with different widths and pitches, grouped to 10 identical trench lines next to each other. Details about the Si/SiO₂ trench pattern fabrication and the InGaAs deposition conditions can be found in [40]. The NR base was always deposited at high substrate temperature (590 °C) with the application of antimonide (Sb) as a surfactant to ensure the NR box formation. The beneficial impact of a surfactant in NRE was already introduced in [40] and is the key to achieve uniform InGaAs NR base lines. For sample 1 the substrate temperature was kept at 590 °C for the deposition of the MQW structure but for sample 2 and 3 the growth temperature of the active MQW region was reduced to 570 °C and 550 °C, respectively, as the modified hetero-structure was containing more integrated compressive strain. All NR samples were capped with an InGaP layer deposited at 600 °C. To be lattice matched, the In-content was adjusted according to the InGaAs NR lattice constant. To vary the In-concentration in the NR base, MQW structure and cap layer of the different samples, the Ga- and In-precursor ratio inside the growth chamber had to be changed. For our chosen InGaAs growth conditions, the NRs on top of 60, 80, 100 and 120 nm wide trenches (with pitch 11 times the trench width) are most suitable for laser device fabrication as the trench aspect ratio is efficiently high to trap all misfit defects and the NR volume is large enough to guide a laser mode in the O-band. We found the crystal quality of the NRs to be comparable for all these trench lines and the NR width and height are increasing for about 11% and 4%, respectively, going from 60 to 100 nm wide trenches. The In-content inside the NR base and QWs might also slightly change with the trench width but this variation is negligible for the following discussion.

The In-concentrations and strain states were determined by high-resolution X-ray diffraction reciprocal space maps (RSMs) around the (224) reflections with an X-ray incident direction parallel and perpendicular to the trench orientation. The crystal quality was inspected by transmission electron microscopy (TEM) applying different imaging conditions to reveal all possible types of defects. Energy-dispersive X-ray spectroscopy (EDS) provided additional feedback about the atomic alloy composition. Photoluminescence (PL) was measured in a

micro-PL set-up with a continuous wave (CW) excitation wavelength of 532 nm. Details about the NR laser fabrication and pump set-up are described later.

3. Results and discussion

3.1. Shifting the nano-ridge emission wavelength to the O-band

In our first hetero-structure design, referred to as sample 1, we grew an InGaAs NR base with 34% In and deposited two QWs with 45% In on top of the NR base. The In-content of the InGaP cap layer is 80% in order to be lattice matched to the free-standing lattice constant of the $\text{In}_{0.34}\text{Ga}_{0.66}\text{As}$ NR base. The implementation of an InGaP cap layer is very important in such a nanometer-scale NR structure to ensure sufficient carrier confinement and to reduce surface recombination [41]. The uniform growth of this InGaAs NR array becomes obvious in Fig. 1(a), which holds a tilted cross-section scanning electron microscopy (SEM) image of sample 1. The false colors indicate the position of the QWs and InGaP cap layer as well as the NR base material.

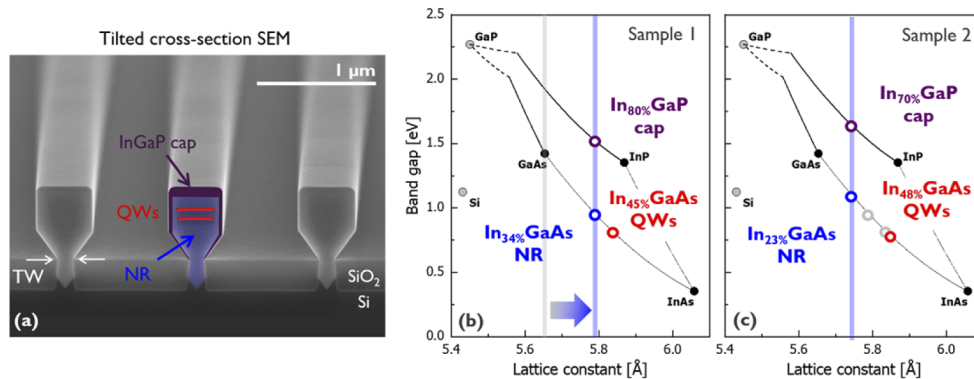


Fig. 1. (a) Tilted cross-section SEM image of sample 1 with a trench width (TW) of 100 nm and a pitch of 1100 nm. The false colors of the middle NR indicate the main NR material and the position of the QWs and the cap layer. (b) and (c) are charts of the band gap versus the III-V lattice constant illustrating the NR layer stack of sample 1 and 2 with open circles. The grey open circles in figure (c) indicate the original composition of sample 1 in (b).

Figure 1 (b) is a chart of the band gap versus the lattice constant for various III-V materials, highlighting the choice of material for sample 1. While the composition of the InGaP cap was chosen to be lattice matched to $\text{In}_{0.34}\text{Ga}_{0.76}\text{As}$, the QWs with 45% In are compressively strained with a lateral strain value ϵ_1 of -0.008, which is beneficial for the laser performance but still reasonably low in value to guarantee full pseudomorphic growth without any misfit defect formation. A RSM of sample 1 around the (224) reflection with an X-ray incident direction parallel to the trench orientation is shown in Fig. 2(a). The (224) reflex of the fully relaxed InGaAs NR base is clearly visible in the RSM. The diffraction signal of the two QWs is weaker due to the limited QW volume with ~ 8 nm layer thickness, but the perfect vertical alignment under the NR reflex in the RSM confirms that the QWs are fully strained to the InGaAs NR base. Table 1 provides a summary of all key parameters of the samples discussed in this investigation.

To explore the optical properties of this new NR laser stack, photoluminescence (PL) measurements were carried out at room temperature. A pronounced PL signal was obtained with rising intensity for an increasing excitation power. In Fig. 2(c) two PL peaks can be identified at 1285 and 1405 nm, which are correlated to the radiative recombination inside the NR base and the QWs, respectively. First of all, this demonstrates that the QW luminescence was successfully red-shifted with this new NR hetero-structure design. Unfortunately, the PL peak intensity of the NR base at 1285 nm is stronger than the PL originating from the QWs at 1405 nm. This is

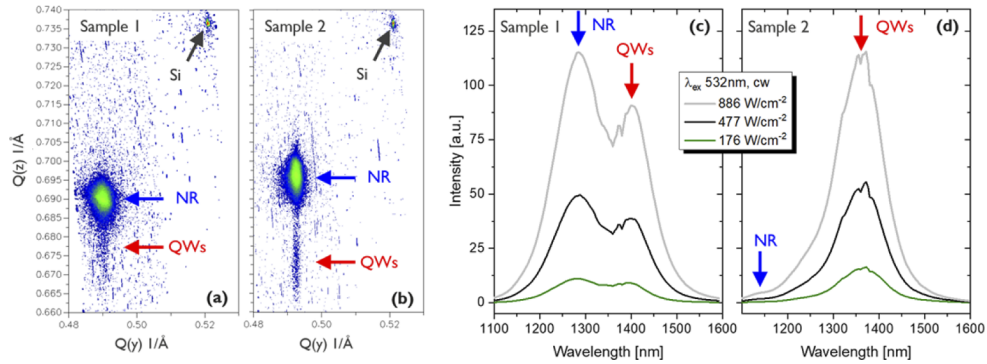


Fig. 2. (a) and (b) are RSMs of sample 1 and 2 around the (224) reflections with an X-ray incident direction parallel to the trench orientation, the x-axis ($Q(y)$) and y-axis ($Q(z)$) correlates with the in plane (along the trench) and out of plane lattice constant. (c) and (d) are the related room temperature PL spectra of sample 1 and 2 for different CW excitation intensities at 532 nm. The NR trench width and pitch of the measured sample areas are 100 and 1100 nm, respectively.

caused by the weak MQW hetero-offset and, hence, insufficient carrier capture inside the QWs, which results in a significant portion of carrier recombination inside the NR base material which is much larger in volume than the QWs.

To strengthen the PL of the QWs, a new NR laser stack was grown with an improved carrier confinement inside the QWs and an additional third QW. In sample 2 the In-content of the three QWs was kept around the same value as in sample 1 with 48% In but the In-concentration of the NR base and, hence, QW barrier was now reduced to 23% so that the MQW hetero-offset is increased. This is a very unique approach to optimize a laser stack, as the base lattice constant is modified rather than the QW composition. In addition, the InGaP cap composition is also adjusted to 70% to ensure lattice-matched growth to the fully relaxed $\text{In}_{0.23}\text{Ga}_{0.77}\text{As}$ NR base.

Figure 1(c) and Fig. 2(b) are the corresponding chart and RSM of sample 2. Because of the larger difference in In-content between the NR base and MQW structure, the diffraction signal of the QWs is more separated from the NR base reflex. Again, the perfect vertical alignment of the QW diffraction signal underneath the NR base reflex proves that the MQW stack is fully strained to the modified $\text{In}_{0.23}\text{Ga}_{0.77}\text{As}$ NR lattice constant. Finally, in the PL spectra of sample 2 only one pronounced emission peak from the QWs is visible at 1370 nm because of the improved carrier capture. Despite the higher QW In-concentration in sample 2 the emission wavelength is slightly blue shifted in comparison to sample 1 due to the larger in plane QW strain ε_2 of -0.017. A flat PL shoulder is faintly recognizable for a high excitation intensity at 1150 nm, which could still originate from the $\text{In}_{0.23}\text{Ga}_{0.77}\text{As}$ NR base material.

Table 1. Summary of the key hetero-structure parameters of sample 1, 2 and 3 based on NRs on top of 100 nm wide trenches with a pitch of 1100 nm. The lateral QW strain ε is defined as $(a_{\text{strained}} - a_{\text{free}})/a_{\text{free}}$ where a_{strained} is the in plane strained lattice constant and a_{free} the unstrained free lattice constant

#	In-content NR base	In-content QWs	QW thickness	Number of QWs	Lateral QW strain $\varepsilon = (a_{\text{strained}} - a_{\text{free}})/a_{\text{free}}$
1	34%	45%	~ 8 nm	2	-0.008
2	23%	48%	~ 8 nm	3	-0.017
3	25%	45%	~ 16 nm	3	-0.014

3.2. Laser structure

In a final optimization loop we further reduced the growth temperature of the MQW structure preventing misfit defect formation to increase the QW thickness to 16 nm, which leads to enhanced modal gain. The change in deposition temperature also resulted in slightly modified In-concentrations and, hence, QW strain for sample 3 (25%, 45% and 72% In for the NR, QWs and cap, strain ϵ_3 of -0.014). Additionally, we introduced n-doping in the InGaAs NR base by incorporating Si during the first NR formation, which is the first step towards current injection and reduces the diffusion of excited holes into the defective trench area.

The structural crystal quality of sample 3 was examined by an in-depth TEM investigation applying different TEM imaging conditions. Efficient misfit defect (MD) trapping of all threading dislocations is observed inside the trench as expected for ART. Inside the NR volume and MQW structure, no indication of MD formation was found in images taken across several NRs and in the 5 μm long TEM lamella along the NR line. Although the defect statistics are very limited in a cross-section TEM study, this first structural feedback confirms that our new laser design concept can be realized with high crystal quality in a hetero-epitaxial integration approach on Si. Figure 3 summarizes the main TEM observations. Figure 3 (a) is an EDS map of the In-La transition which reveals the In distribution across the complete NR. The main NR volume consisting of 25% InGaAs induces a certain In-La intensity contrast. The n-doped part of the NR is marked with a white dashed line and stops below the first QW position. The QWs and InGaP cap layer are brighter in EDS intensity due to the higher In content compared to the main NR with 45% and 72%, respectively. A closer look at the InGaAs material in the top region of the trench reveals the appearance of two dark lines, which trace the evolution of the top two NR box corners during growth. These are two Ga rich (In poor) veins caused by the facet dependent group III incorporation in NRE. This kind of vein formation was found before in InGaAs NRE and is discussed in-depth in [40]. As long as this composition gradient is low in value and does not induce any misfit defects, which is the case here, it does not have a detrimental impact on our device performance. Figure 3 (b) is a high-angle annular dark-field scanning TEM (HAADF-STEM) image which is very sensitive to alloy compositions. It emphasizes the main hetero-layer features as already identified in the EDS map. Since all facets of the NR structure are exposed during SAG, the InGaAs QW material is also deposited on the NR sidewalls. This is evident from the bright material contrast in the zoomed-in HAADF-STEM images of Fig. 3(c). This {110} sidewall QWs are thick enough to bond an electron-hole pair and, hence, could contribute to PL but the competing 16 nm thick QWs on the top (001) plane seems to be more efficient in carrier capture as we saw only one distinct peak in PL measurements. The thin InGaP layer also noticeable in Fig. 3(c) acts as a passivation layer along the {111} facets. The course of trapped misfit dislocations inside the trench are clearly visible as bright lines in the dark-field scanning TEM (DF-STEM) image of Fig. 3(d). The bright region along the two {111} III-V/Si interfaces is caused by a dense array of 60° misfit dislocations releasing the main mismatch strain [42].

A HAADF-STEM and an annular bright-field scanning TEM (ABF-STEM) image in a cut direction along the NR line are shown in Fig. 3(e) and (f), respectively. The HAADF-STEM image reveals again the different III-V materials and underlines the very uniform multi-layer structure with abrupt interfaces. The ABF-STEM image clearly visualizes the efficiency of ART as all dark and blurry lines, which are induced by the strain fields of threading dislocations, end inside the trenches. The only defects we still find in our NR structure are planar defects (PD) along the {111} planes perpendicular to the trench orientation, such as stacking faults and micro twins (MT). These PDs are initiated at the III-V/Si interface and infiltrate the complete NR structure as they are not blocked by ART. Stacking faults and MTs are mainly caused by a non-optimal InGaAs seed layer and/or residues on the Si surface. Figure 3(g) is a magnified (220) bright-field TEM (BF-TEM) image of the trench region where a MT is clearly distinguishable

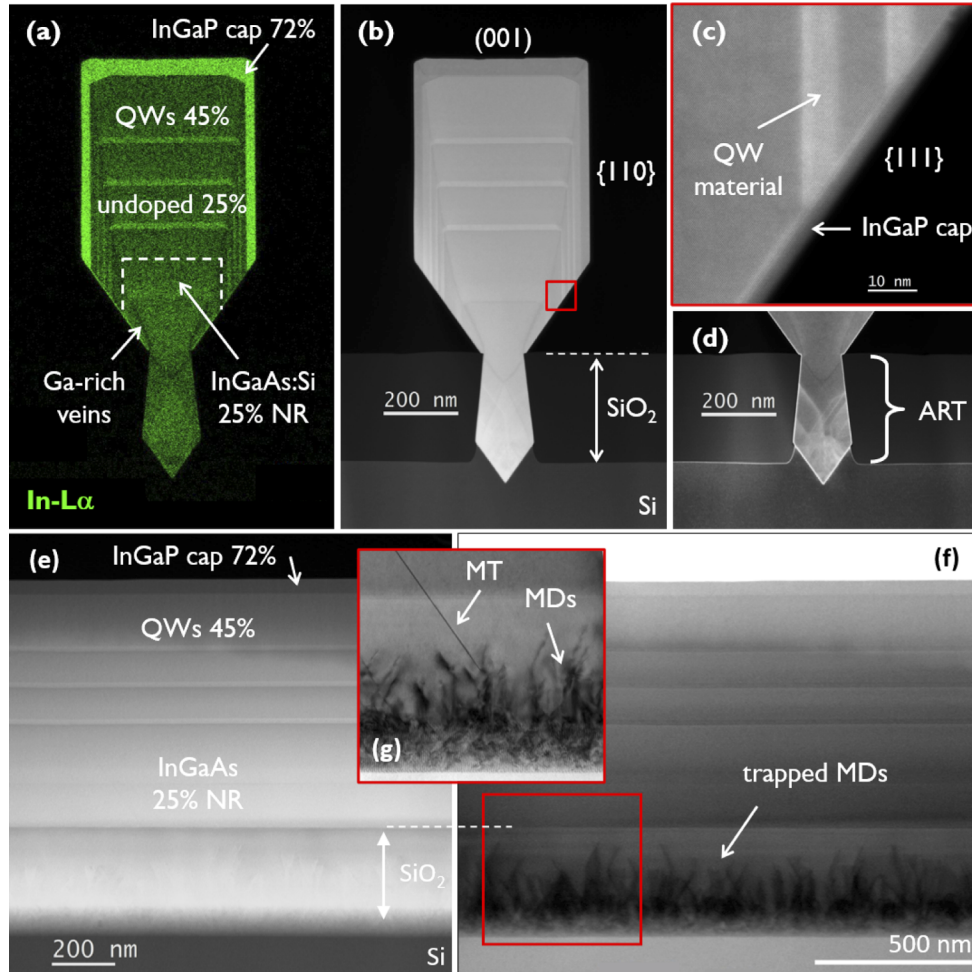


Fig. 3. (a) is an EDS map of the In-L α transition across the NR line. The dashed white line indicates the extent of the n-doped InGaAs NR. (b) is the corresponding HAADF-STEM image which is sensitive to the alloy composition. (c) is a magnified HAADF-STEM picture of the region marked with a red rectangle in figure (b). (d) is a DF-STEM image of the trench region where strain fields, induced by misfit dislocation defects, lead to white contrast lines. (e), (g) and (f) are TEM images in a cut direction along the NR trench line. (e) is a HAADF-STEM image, (f) is an ABF-STEM image and (g) a magnified (220) BF-TEM image of the trench region indicated in (f) revealing more clearly a micro twin (MT) next to trapped misfit defects (MDs). The height of the SiO₂ layer is marked by the white dash line. Strain fields of misfit dislocations cause dark and blurry lines in BF-STEM pictures (f) and are only present inside the trench.

next to the trapped misfit defects (MDs). Inside a bulk layer, PDs are accompanied by partial dislocations at each end of the plane. In the case of our three-dimensional NR structures, PDs usually reach the $\{110\}$ NR side surface. Hence, no partial dislocations should be present inside the NR volume. For this reason, we expect a less destructive impact of PDs on the NR device performance.

3.3. Laser processing and characterization

The fabrication of a metallic grating (MG) on top of the nano-ridges results in a loss-coupled DFB NR laser. This device concept was earlier successfully used for GaAs based NR lasers [37]. The optimal duty cycle of the grating (portion of the metal width within one grating period) was defined by simulations to find a good trade-off between coupling strength and cavity losses of the optical mode inside the metal. The grating period ranges from 190 to 210 nm to account for any variation in NR dimension as a function of the trench width and pitch. 10 μm separated from the DFB grating a second order grating was fabricated to couple light vertically out from the substrate. This allows for the use of a standard micro-PL set-up. Two NR lines out of a group of 10 are processed to a DFB laser whereas the remaining NRs are capped with a metal line (ML) to reduce background PL as shown in the concept drawing of Fig. 4(a).

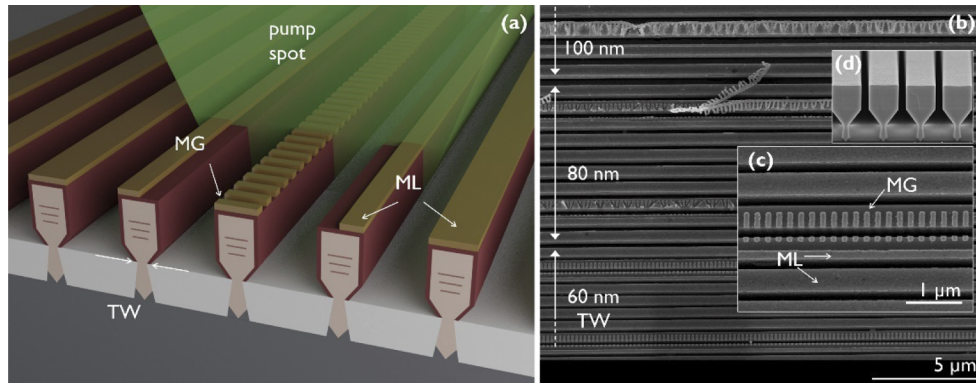


Fig. 4. (a) Concept drawing of the metal loss-coupled DFB NR laser. (b) Top-view SEM image of a processed die area including NR lines based on 60, 80 and 100 nm trench width (TW). (c) is a magnified top-view SEM image of 60 nm NR lines. (d) is a tilted cross-section SEM image of unprocessed 60 nm NR lines. The scale bar in (c) counts also for image (d). The metal lift-off was only successful for the 60 nm NR lines. The metal grating (MG) is slightly misaligned and touches the adjacent NR. A continuous metal line (ML) is placed on top of the surrounding NRs to reduce background PL during pump experiments.

The device fabrication starts with an e-beam lithography step, followed by the deposition of a 5/40 nm Ti/Au layer through evaporation and a final lift-off. During the fabrication, we observed that the e-beam resist thickness varied strongly with the NR size and separation. As a result, the lift-off was only optimal for NRs on top of 60 nm wide trenches with a low pitch of 660 nm. Figure 4(b) is a top-view SEM image which covers the NR lines with 60, 80 and 100 nm trench width (TW), unmistakably revealing the lift-off issues for the wider trench lines. Only for 60 nm NR lines the grating is clearly distinguishable, although the grating was not perfectly centered on top of the NR as shown in Fig. 4(c), which is a magnified top-view SEM image. The measured grating duty cycle of 49% is larger than our target value of 37%. Figure 4(d) is a cross-section SEM images of the NR array on top of 60 nm wide trenches. Unfortunately, the low pitch of only 660 nm results in a small spacing between the NRs. A simulation indicates that a very small portion of the basic TE mode leaks into the neighboring NRs, introducing an additional not fully

negligible loss path in these 60 nm TW DFB lasers, which is not the case for our NR lines with the wider pitch.

Despite the non-perfect grating fabrication and NR spacing, devices based on the 60 nm TW were optically pumped from the top with a pulsed laser at 532 nm (7 ns pulse width, 1000 Hz repetition). To excite only one DFB laser at a time, a slit was used to reduce the lateral extension of the pump spot to 6–8 μm . The pump spot covers about 100 μm length of the laser grating as well as the out-coupling grating to prevent absorption in this region.

The emitted light detected from the processed NR device as a function of the peak pump intensity reveals a clear threshold behavior as shown in Fig. 5(a) on a linear scale as expected for laser operation. On the log-log scale in Fig. 5(b) a pronounced S-shape is recognizable, which indicates the transition from spontaneous emission (SE) via amplified SE to stimulated emission. Figure 5(c) holds three PL spectra, one collected below and two above the threshold. A clear lasing peak evolves at 1292 nm above threshold. With increasing pump intensity, the broad PL signal also slightly increases, especially around 1100 nm. This indicates that an insufficient carrier pinning after reaching the threshold causes a growing radiative recombination in the main $\text{In}_{0.25}\text{Ga}_{0.75}\text{As}$ NR material. This is the first NR laser demonstration based on an $\text{In}_{0.45}\text{GaAs}_{0.55}/\text{In}_{0.25}\text{Ga}_{0.75}\text{As}$ MQW hetero-structure emitting in the O-band. The threshold value of $8 \text{ kW}/\text{cm}^2$ is comparable to what has been observed for the first metal loss-coupled DFB NR laser emitting at 1020 nm based on GaAs NRs [37].

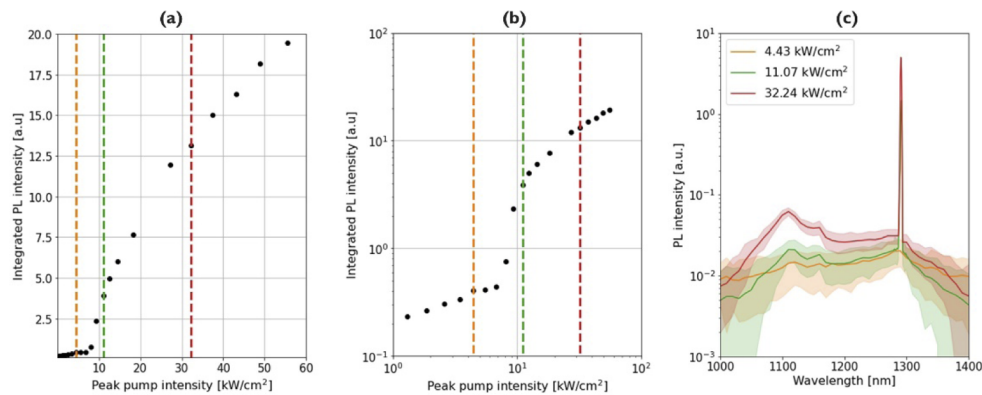


Fig. 5. Integrated PL intensity versus the peak pump intensity on a linear scale (a) and on a log-log scale (b) obtained at room temperature. The PL integration range is from 1280 to 1300 nm. Figure (c) holds three emission spectra, one obtained with a peak pump intensity below the threshold and two spectra measured above threshold. The shaded region around the continuous line represents the error bar on the PL measurement. The lasing peak is at 1292 nm. The vertical dashed lines in (a) and (b) mark the chosen pump intensity values for the spectra in (c). The investigated DFB NR laser is based on 60 nm wide trenches with a measured metal grating period of 198 nm.

In a second device process iteration the alignment of the grating was corrected to perfectly cover the width of an isolated NR as shown in Fig. 6(a). Figure 6(b) and (c) hold the corresponding graphs of the integrated PL intensity and emission spectra of this optimized 2nd generation DFB NR laser. This improved grating fabrication results in a reduced threshold pump intensity below $2 \text{ kW}/\text{cm}^2$. Since such an isolated process improvement resulted already in a clearly decreased threshold, the performance of our current device stack is most likely not limited by the NR crystal quality but rather by the still immature metal grating process. Further optimization of the DFB fabrication together with the choice of NRs with wider separation should result in even better NR laser performance.

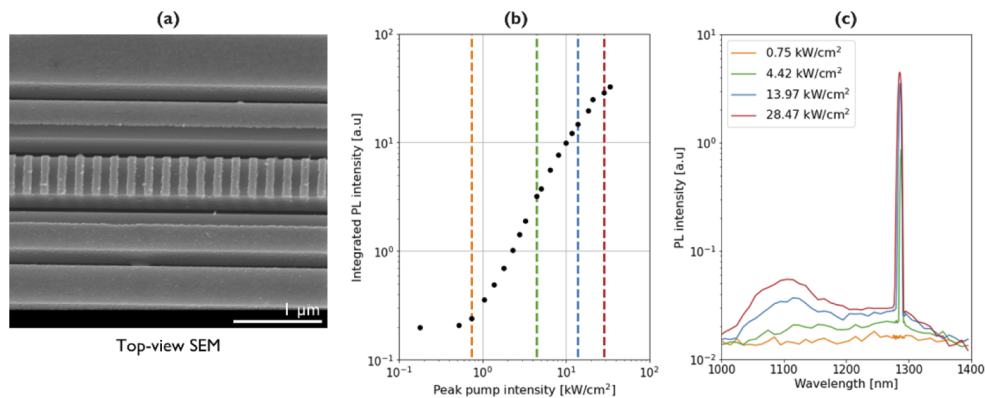


Fig. 6. (a) is a top-view SEM image of a 2nd generation DFB NR laser based on 60 nm trench width and a measured metal grating period of 203 nm. (b) is the integrated PL intensity (range 1275–1295 nm) versus the peak pump intensity on a log-log scale and (c) summarizes several emission spectra obtain below and above threshold. The lasing peak is at 1289 nm. The vertical dashed lines in (b) indicate the applied peak pump intensity for the different spectra in (c).

4. Conclusion

The monolithic deposition of fully relaxed InGaAs NRs on Si substrates leads to an additional device design space, as the fundamental lattice constant can be freely adjusted by the NR composition. This allows for the pseudomorphic growth of compressively strained InGaAs QWs with $\sim 45\%$ In on top of an InGaAs NR base (with lower In content) emitting photons in the O-band. We explored this new NR design concept where we kept the QW composition constant but tuned the InGaAs NR base composition between 20–35% to realize a NR laser for applications in silicon photonics. Increasing the hetero-offset between the QWs and barrier by decreasing the In content of the NR base below $\sim 25\%$ resulted in a pronounced single peak O-band luminescence. A detailed TEM investigation did not reveal any indication of misfit defect formation inside the active NR volume. Finally, an $\text{In}_{0.45}\text{Ga}_{0.55}\text{As}/\text{In}_{0.25}\text{Ga}_{0.75}\text{As}$ device stack with an $\text{In}_{0.72}\text{Ga}_{0.28}\text{P}$ cap layer was used to fabricate a metal grating loss-coupled DFB NR laser. Optically pumped laser operation at room temperature emitting around 1300 nm confirms the excellent NR crystal quality and its huge potential as a monolithic integrated laser on silicon. Moreover the first laser demonstration applying such a novel hetero-structure emphasizes the strength of this new design space. Indeed, this device approach based on NRE of an InGaAs alloy is not limited to an operation wavelength in the O-band but enables even longer emission wavelengths, e.g., for telecom and emerging infrared sensing applications in silicon photonics.

Funding. Fonds Wetenschappelijk Onderzoek (1SB9921N).

Acknowledgments. This work was supported by imec's industry-affiliation Optical I/O R&D Program. The first author would like to acknowledge the Flemish Research Council (FWO) for his Ph.D. scholarship (1SB9921N).

Disclosures. The authors declare no conflicts of interest.

Data availability. Data underlying the results presented in this paper are not publicly available at this time but may be obtained from the authors upon reasonable request.

References

1. M. Pantouvaki, S. A. Srinivasan, Y. Ban, P. De Heyn, P. Verheyen, G. Lepage, H. Chen, J. De Coster, N. Golshani, S. Balakrishnan, P. Absil, and J. Van Campenhout, "Active Components for 50 Gb/s NRZ-OOK Optical Interconnects in a Silicon Photonics Platform," *J. Lightwave Technol.* **35**(4), 631–638 (2017).
2. N. Margalit, C. Xiang, S. M. Bowers, A. Bjorlin, R. Blum, and J. E. Bowers, "Perspective on the future of silicon photonics and electronics," *Appl. Phys. Lett.* **118**(22), 220501 (2021).

3. C. Minkenberg, R. Krishnaswamy, A. Zilkie, and D. Nelson, "Co-packaged datacenter optics: Opportunities and challenges," *Iet Optoelectron.* **15**, 77–91 (2021).
4. Z. Wang and M. Menenti, "Challenges and Opportunities in Lidar Remote Sensing," *Front. Remote Sens.* **2**(March), 1–8 (2021).
5. X. Sun, L. Zhang, Q. Zhang, and W. Zhang, "Si photonics for practical LiDAR solutions," *Appl. Sci.* **9**(20), 11 (2019).
6. E. Luan, H. Shoman, D. M. Ratner, K. C. Cheung, and L. Chrostowski, "Silicon photonic biosensors using label-free detection," *Sensors (Switzerland)* **18**(10), 1–42 (2018).
7. H. Lin, Z. Luo, T. Gu, L. C. Kimerling, K. Wada, A. Agarwal, and J. Hu, "Mid-infrared integrated photonics on silicon: A perspective," *Nanophotonics* **7**(2), 393–420 (2017).
8. R. Wang, A. Vasiliev, M. Muneeb, A. Malik, S. Sprengel, G. Boehm, M. C. Amann, I. Šimonytė, A. Vizbaras, K. Vizbaras, R. Baets, and G. Roelkens, "III–V-on-silicon photonic integrated circuits for spectroscopic sensing in the 2–4 μm wavelength range," *Sensors (Switzerland)* **17**(8), 12 (2017)..
9. S. Lin, X. Zheng, J. Yao, S. S. Djordjevic, J. E. Cunningham, J-H. Lee, I. Shubin, Y. Luo, J. Bovington, D. Y. Lee, H. D. Thacker, K. Raj, and A. V. Krishnamoorthy, "Efficient, tunable flip-chip-integrated III-V / Si hybrid external-cavity laser array," *Opt. Express* **24**(19), 21454–21462 (2016).
10. S. Bao, Y. Wang, K. Lina, L. Zhang, B. Wang, W. A. Sasangka, K. E. K. Lee, S. J. Chua, J. Michel, E. Fitzgerald, C. S. Tan, and K. H. Lee, "A review of silicon-based wafer bonding processes, an approach to realize the monolithic integration of Si-CMOS and III-V-on-Si wafers," *J. Semicond.* **42**(2), 023106 (2021)..
11. C. Xiang, W. Jin, D. Huang, M. A. Tran, J. Guo, Y. Wan, W. Xie, G. Kurczveil, A. Netherton, D. Liang, H. Rong, and J. E. Bowers, "High-performance silicon photonics using heterogeneous integration," *IEEE J. Sel. Top. Quantum Electron.* **10**(Section II), 1 (2021).
12. Y. Hu, D. Liang, and R. G. Beausoleil, "An advanced iii-v-on-silicon photonic integration platform," *Opto-Electronic Adv.* **4**(9), 1–14 (2021).
13. J. Zhang, G. Muliuk, J. Juvert, S. Kumari, J. Goyvaerts, B. Haq, C. Op de Beeck, B. Kuyken, G. Morthier, D. Van Thourhout, R. Baets, G. Lepage, P. Verheyen, J. Van Campenhout, A. Gocalinska, J. O'Callaghan, E. Pelucchi, K. Thomas, B. Corbett, A. J. Trindade, and G. Roelkens, "III-V-on-Si photonic integrated circuits realized using micro-transfer-printing," *APL Photonics* **4**(11), 110803 (2019).
14. G. Wang, R. Loo, E. Simoen, L. Souriau, M. Caymax, M. M. Heyns, and B. Blanpain, "A model of threading dislocation density in strain-relaxed Ge and GaAs epitaxial films on Si (100)," *Appl. Phys. Lett.* **94**(10), 102115 (2009).
15. E. Tournie, L. Cerutti, J. B. Rodriguez, H. Y. Liu, J. Wu, and S. M. Chen, "Metamorphic III-V semiconductor laser grown on silicon," *MRS Bull.* **41**(3), 218–223 (2016).
16. B. Kunert, Y. Mols, M. Baryshnikova, N. Waldron, A. Schulze, and R. Langer, "How to control defect formation in monolithic III/V hetero-epitaxy on (100) Si? A critical review on current approaches," *Semicond. Sci. Technol.* **33**(9), 93002 (2018).
17. J. S. Park, M. Tang, S. Chen, and H. Liu, "Heteroepitaxial growth of iii-v semiconductors on silicon," *Crystals* **10**(12), 1–36 (2020).
18. J. Selvidge, J. Norman, E. T. Hughes, C. Shang, D. Jung, A. A. Taylor, M. J. Kennedy, R. Herrick, J. E. Bowers, and K. Mukherjee, "Defect filtering for thermal expansion induced dislocations in III-V lasers on silicon," *Appl. Phys. Lett.* **117**(12), 122101 (2020).
19. C. Shang, J. Selvidge, E. Hughes, J. C. Norman, A. A. Taylor, A. C. Gossard, K. Mukherjee, and J. E. Bowers, "A Pathway to Thin GaAs Virtual Substrate on On-Axis Si (001) with Ultralow Threading Dislocation Density," *Phys. Status Solidi Appl. Mater. Sci.* **218**(3), 1–9 (2021).
20. C. Shang, Y. Wan, J. Selvidge, E. Hughes, R. Herrick, K. Mukherjee, J. Duan, F. Grillot, W. W. Chow, and J. E. Bowers, "Perspectives on Advances in Quantum Dot Lasers and Integration with Si Photonic Integrated Circuits," *ACS Photonics* **5**, 2555–2566 (2021).
21. K. Mukherjee, J. Selvidge, D. Jung, J. Norman, A. A. Taylor, M. Salmon, A. Y. Liu, J. E. Bowers, and R. W. Herrick, "Recombination-enhanced dislocation climb in InAs quantum dot lasers on silicon," *J. Appl. Phys.* **128**(2), 025703 (2020).
22. Z. Liu, M. Martin, T. Baron, S. Chen, A. Seeds, R. Penty, I. White, H. Liu, C. Hantschmann, M. Tang, Y. Lu, J. S. Park, M. Liao, S. Pan, A. Sanchez, and R. Beanland, "Origin of Defect Tolerance in InAs/GaAs Quantum Dot Lasers Grown on Silicon," *J. Lightwave Technol.* **38**(2), 240–248 (2020).
23. J. C. Norman, R. P. Mirin, and J. E. Bowers, "Quantum dot lasers—History and future prospects," *J. Vac. Sci. Technol. A* **39**(2), 020802 (2021).
24. R. Herrick and O. Ueda, "Reliability of Semiconductor Lasers and Optoelectronic Devices," 1st Editio., Robert Herrick and Osamu Ueda, Eds. Woodhead Publishing, (2021). p. 334.
25. J. S. Park, J. Bai, M. Curtin, B. Adekore, M. Carroll, and A. Lochtefeld, "Defect reduction of selective Ge epitaxy in trenches on Si(001) substrates using aspect ratio trapping," *Appl. Phys. Lett.* **90**(5), 43–46 (2007).
26. H. Schmid, M. Borg, K. Moselund, L. Gignac, C. M. Breslin, J. Bruley, D. Cutaia, and H. Riel, "Template-assisted selective epitaxy of III-V nanoscale devices for co-planar heterogeneous integration with Si," *Appl. Phys. Lett.* **106**(23), 233101 (2015).

27. N. Waldron, C. Merckling, L. Teugels, P. Ong, F. Sebaai, K. Barla, N. Collaert, and V. Y. Thean, "Replacement fin processing for III-V on Si: From FinFets to nanowires," *Solid. State. Electron.* **115**, 81–91 (2016).
28. S. Wirths, B. F. Mayer, H. Schmid, M. Sousa, J. Gooth, H. Riel, and K. E. Moselund, "Room-Temperature Lasing from Monolithically Integrated GaAs Microdisks on Silicon," *ACS Nano* **12**, 2169–2175 (2018).
29. Y. Han and K. M. Lau, "III-V lasers selectively grown on (001) silicon," *J. Appl. Phys.* **128**(20), 200901 (2020).
30. Y. Han, Y. Xue, Z. Yan, and K. M. Lau, "Selectively Grown III-V Lasers for Integrated Si-Photonics," *J. Light. Technol.* **39**(4), 940–948 (2021).
31. X. Yuan, D. Pan, Y. Zhou, X. Zhang, K. Peng, B. Zhao, M. Deng, J. He, H. H. Tan, and C. Jagadish, "Selective area epitaxy of III-V nanostructure arrays and networks: Growth, applications, and future directions," *Appl. Phys. Rev.* **8**(2), 021302 (2021).
32. B. Kunert, W. Guo, Y. Mols, R. Langer, and K. Barla, "Integration of III/V Hetero-structures by Selective Area Growth on Si for Nano- and Optoelectronic," *ECS Trans.* **75**(8), 409–419 (2016).
33. D. Van Thourhout, Y. Shi, M. Baryshnikova, Y. Mols, N. Kuznetsova, Y. De Koninck, M. Pantouvaki, J. Van Campenhout, R. Langer, and B. Kunert, "Nano-ridge laser monolithically grown on (001) Si," in *Semiconductors and Semimetals*, *Future Directions in Silicon Photonics* **101**, 283–304 (2019).
34. M. Baryshnikova, Y. Mols, Y. Ishii, R. Alcotte, H. Han, T. Hantschel, O. Richard, M. Pantouvaki, J. Van Campenhout, D. Van Thourhout, R. Langer, and B. Kunert, "Nano-Ridge Engineering of GaSb for the Integration of InAs/GaSb Heterostructures on 300 mm (001) Si," *Crystals* **10**(4), 330 (2020).
35. Y. Shi, Z. Wang, J. Van Campenhout, M. Pantouvaki, W. Guo, B. Kunert, and D. Van Thourhout, "Optical pumped InGaAs/GaAs nano-ridge laser epitaxially grown on a standard 300-mm Si wafer," *Optica* **4**(12), 1468 (2017).
36. Y. Shi, B. Kunert, Y. De Koninck, M. Pantouvaki, J. Van Campenhout, and D. Van Thourhout, "Novel adiabatic coupler for III-V nano-ridge laser grown on a Si photonics platform," *Opt. Express* **27**(26), 37781 (2019).
37. Y. Shi, M. Pantouvaki, J. Van Campenhout, D. Colucci, M. Baryshnikova, B. Kunert, and D. Van Thourhout, "Loss-coupled DFB nano-ridge laser monolithically grown on a standard 300-mm Si wafer," *Opt. Express* **29**(10), 14649–14657 (2021).
38. C. I. Ozdemir, Y. De Koninck, D. Yudistira, N. Kuznetsova, M. Baryshnikova, D. Van Thourhout, B. Kunert, M. Pantouvaki, and J. Van Campenhout, "Low Dark Current and High Responsivity 1020 nm InGaAs/GaAs Nano-Ridge Waveguide Photodetector Monolithically Integrated on a 300-mm Si Wafer," *J. Lightwave Technol.* **39**(16), 5263–5269 (2021).
39. Y. Mols, J. Bogdanowicz, P. Favia, P. Lagrain, W. Guo, H. Bender, and B. Kunert, "Structural analysis and resistivity measurements of InAs and GaSb fins on 300 mm Si for vertical (T)FET," *J. Appl. Phys.* **125**(24), 13 (2019).
40. B. Kunert, R. Alcotte, Y. Mols, M. Baryshnikova, N. Waldron, N. Collaert, and R. Langer, "Application of an Sb Surfactant in InGaAs Nano-ridge Engineering on 300 mm Silicon Substrates," *Cryst. Growth Des.* **21**(3), 1657–1665 (2021).
41. Y. Shi, L. C. Kreuzer, N. C. Gerhardt, M. Pantouvaki, J. Van Campenhout, M. Baryshnikova, R. Langer, D. Van Thourhout, and B. Kunert, "Time-resolved photoluminescence characterization of InGaAs/GaAs nano-ridges monolithically grown on 300 mm Si substrates," *J. Appl. Phys.* **127**(10), 103104 (2020).
42. W. Guo, Y. Mols, J. Belz, A. Beyer, K. Volz, A. Schulze, R. Langer, and B. Kunert, "Anisotropic relaxation behavior of InGaAs/GaAs selectively grown in narrow trenches on (001) Si substrates," *J. Appl. Phys.* **122**(2), 025303 (2017).